Electrostatic Turbulence and Debye-scale Structures in Collisionless Shocks

R. Wang[1,2] , I. Y. Vasko[1] , F. S. Mozer[1] , S. D. Bale[1,2] , A. V. Artemyev[3,4], J. W. Bonnell[1], R. Ergun[5], B. Giles[6],
P.-A. Lindqvist[7], C. T. Russell[4] , and R. Strangeway[4]
[1] Space Sciences Laboratory, University of California, Berkeley, CA 94720, USA; rachel_w@berkeley.edu
[2] Physics Department, University of California, Berkeley, CA 94720, USA
[3] Space Research Institute of Russian Academy of Sciences, Moscow, Russia
[4] Institute of Geophysics and Planetary Sciences, University of California, Los Angeles, CA, USA
[5] University of Colorado at Boulder, Boulder, CO, USA
[6] NASA, Goddard Space Flight Center, Greenbelt, MD, USA
[7] Royal Institute of Technology, Stockholm, Sweden

Abstract

We present analysis of more than 100 large-amplitude bipolar electrostatic structures in a quasi-perpendicular supercritical Earth's bow shock crossing, measured by the *Magnetospheric Multiscale* spacecraft. The occurrence of the bipolar structures is shown to be tightly correlated with magnetic field gradients in the shock transition region. The bipolar structures have negative electrostatic potentials and spatial scales of a few Debye lengths. The bipolar structures propagate highly oblique to the shock normal with velocities (in the plasma rest frame) of the order of the ion-acoustic velocity. We argue that the bipolar structures are ion phase space holes produced by the two-stream instability between incoming and reflected ions. This is the first identification of the ion two-stream instability in collisionless shocks.

Unified Astronomy Thesaurus concepts: Astrophysical processes (104)

1. Introduction

Supercritical quasi-perpendicular shocks are of interest because of relatively efficient electron acceleration in the shock transition region as inferred from observations in the Earth's bow shock (Gosling et al. 1989; Oka et al. 2006) and astrophysical shocks (e.g., Bamba et al. 2003; van Weeren et al. 2010). In supercritical quasi-perpendicular shocks, the reflection of a fraction of incoming ions (e.g., Leroy et al. 1982) gives rise to various wave activities potentially involved in electron acceleration (e.g., Papadopoulos 1985). Numerical simulations demonstrated that, at high Mach numbers, electrostatic turbulence driven by the Buneman instability may provide efficient electron acceleration in the shock transition region (e.g., Cargill & Papadopoulos 1988; Hoshino & Shimada 2002; Schmitz et al. 2002; Shimada & Hoshino 2004; Amano & Hoshino 2009). A similar process of electron acceleration by electrostatic turbulence may operate at lower Mach numbers typical in the Earth's bow shock (e.g., simulations by Umeda et al. 2009). Nevertheless, the lack of detailed experimental analysis of the origin of electrostatic turbulence in collisionless shocks hinders the quantification of the efficiency of electron acceleration under realistic conditions.

The Earth's bow shock is a natural laboratory for probing the microphysics of supercritical collisionless shocks, because the Alfvén Mach number of the solar wind flow typically exceeds the second critical value, $M_A \gtrsim 3$ (e.g., Kennel et al. 1985). The in situ measurements in the Earth's bow shock showed that electric and magnetic field fluctuations are electromagnetic below a few hundred Hz and mostly electrostatic at higher frequencies (Rodriguez & Gurnett 1975; Mozer & Sundkvist 2013). The measurements of electric and magnetic field waveforms demonstrated that the electromagnetic fluctuations correspond to whistler waves (e.g., Wilson et al. 2014; Oka et al. 2017), while the electrostatic turbulence corresponds to

ion-acoustic waves (Balikhin et al. 2005; Hull et al. 2006; Goodrich et al. 2018) and bipolar electrostatic structures (Bale et al. 1998, 2002). The bipolar structures were interpreted in terms of electron phase space holes, as electrostatic structures produced in a nonlinear stage of various electron streaming instabilities (e.g., Schamel 1986; Hutchinson 2017), and involved in the original scenario of electron surfing acceleration in high Mach number shocks (Hoshino & Shimada 2002; Schmitz et al. 2002). However, until recently, spacecraft measurements did not allow the resolution of the nature and generation mechanisms of the bipolar structures in the Earth's bow shock.

The recently launched *Magnetospheric Multiscale* (*MMS*) spacecraft (Burch et al. 2016) has allowed us to probe the Earth's bow shock with unprecedented temporal resolution and 3D electric field measurements. The analysis of about 20 bipolar structures measured in a particular Earth's bow shock crossing showed that these structures are not electron phase space holes because they have negative electrostatic potentials (Vasko et al. 2018). In this Letter, we present a statistical analysis of more than 100 bipolar structures measured in the shock transition region of a particular Earth's bow shock crossing. We argue that the bipolar structures are ion phase space holes produced by the two-stream instability between incoming and reflected ions in the shock transition region. The implications for the electron surfing acceleration in collisionless shocks are discussed.

2. Observations

We consider the Earth's bow shock crossing by the four *MMS* spacecraft on 2017 November 2 around 06:03:00 UT. We use the DC-coupled magnetic field (128 samples s⁻¹) provided by Digital and Analogue Fluxgate Magnetometers (Russell et al. 2016), AC-coupled electric fields (8192 samples s⁻¹) provided by Axial Double Probe (Ergun et al. 2016) and Spin-
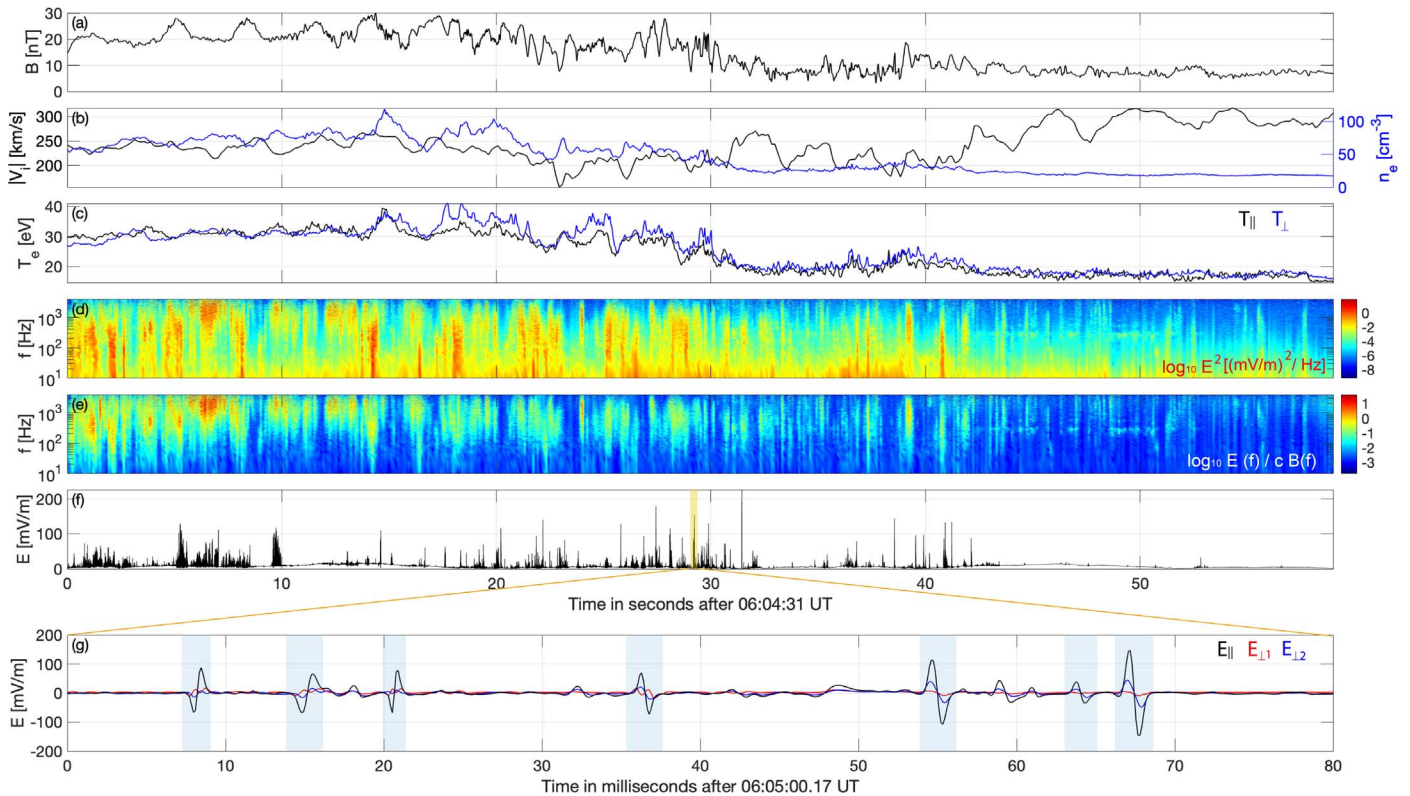
Figure 1. Overview of the Earth's bow shock crossing by the *Magnetospheric Multiscale* spacecraft on 2017 November 2. The panels present measurements of *MMS4*, while other three spacecraft, being located within a few tens of kilometers, provide essentially identical overviews: (a) the magnitude of a quasi-static magnetic field measured at 128 samples s^{-1}; (b) the electron density (0.03 s cadence) and the magnitude of the ion bulk velocity (0.15 s cadence); (c) electron temperatures (0.03 cadence) parallel and perpendicular to a local quasi-static magnetic field; (d) total power spectral density (PSD) $E^2(f)$ of the electric field fluctuations (8192 samples s^{-1}) computed using 0.1 s sliding window, where f denotes frequency (similar PSD $B^2(f)$ was computed for the magnetic field fluctuations measured at 8192 samples s^{-1}); (e) the ratio $E(f)/cB(f)$ between PSDs of electric and magnetic field fluctuations (c is the speed of light), where higher values above a few hundred Hz indicate that the electric field fluctuations at those frequencies tend to be electrostatic (in accordance with Rodriguez & Gurnett 1975); (f) the amplitude of the electric field fluctuations measured at 8192 samples s^{-1}; (g) an expanded view of three electric field components measured over 0.08 s interval highlighted in panel (f), where $E_{\parallel}$ is the electric field component parallel to a local quasi-static magnetic field, while $E_{\perp 1}$ and $E_{\perp 2}$ are corresponding perpendicular components.

Plane Double Probe (Lindqvist et al. 2016), AC-coupled magnetic fields (8192 samples s^{-1}) provided by the Search Coil magnetometer (Le Contel et al. 2016), electron moments (0.03 s cadence) and ion moments (0.15 s cadence) provided by the Fast Plasma Investigation instrument (Pollock et al. 2016). The electric field is measured by four voltage-sensitive spherical probes on 60 m antennas in the spacecraft spin plane (almost in the ecliptic plane) along with two probes on roughly 15 m axial antennas along the spin axis (almost perpendicular to the ecliptic plane). The voltages of the opposing probes measured with respect to the spacecraft are used to estimate the direction of propagation, velocity, and other parameters of bipolar electrostatic structures (see Vasko et al. 2018 for methodology details). We determine the normal to the shock in the Geocentric Solar Ecliptic (GSE) coordinate system with the z-axis perpendicular to the ecliptic plane, the x-axis pointing to the Sun, and the y-axis completing the right-hand coordinate system.

Figure 1 presents a summary of the Earth's bow shock crossing as measured on board *MMS4*. The other *MMS* spacecraft being located within about 20 km of *MMS4* provide almost identical overviews of the shock. The shock transition region can be seen in panel (a) by the magnetic field increase from about 7 nT in the upstream region to about 20 nT in the downstream region. There is an associated deceleration of incoming solar wind ions and an increase of the plasma density

from the upstream value of 16 cm^{-3} to the downstream value of 60 cm^{-3} as shown in panel (b). The electron heating in the shock transition region is essentially isotropic, that is, parallel and perpendicular electron temperatures are almost identical as shown in panel (c). The electron temperature increases from about 15 eV in the upstream region to about 30 eV in the downstream region. The ion temperature in the upstream region is not well measurable by *MMS*, while the *Wind* spacecraft[8] provides an estimate of 6 eV.

The upstream and downstream values of the quantities presented in panels (a) and (b) are used for estimating the normal to the shock and velocity of the shock in the spacecraft frame using the Rankine–Hugoniot conditions (Vinas & Scudder 1986). We have found that in the GSE coordinate system the normal to the shock is $n \approx (0.81, 0.56, 0.2)$ and the shock propagates with the velocity of 38 km s^{-1} in the direction opposite to the normal, that is, toward the Earth. The shock is quasi-perpendicular where the angle between the normal and the upstream magnetic field is $\theta_{Bn} \approx 96°$. In the rest frame of the shock, the ion bulk velocity along the normal decreases from about 200 km s^{-1} in the upstream region to about 70 km s^{-1} in the downstream region (not shown here). The upstream velocity of 200 km s^{-1} corresponds to the Alfvén Mach number $M_A \approx 5.4$. Thus, the considered shock is a
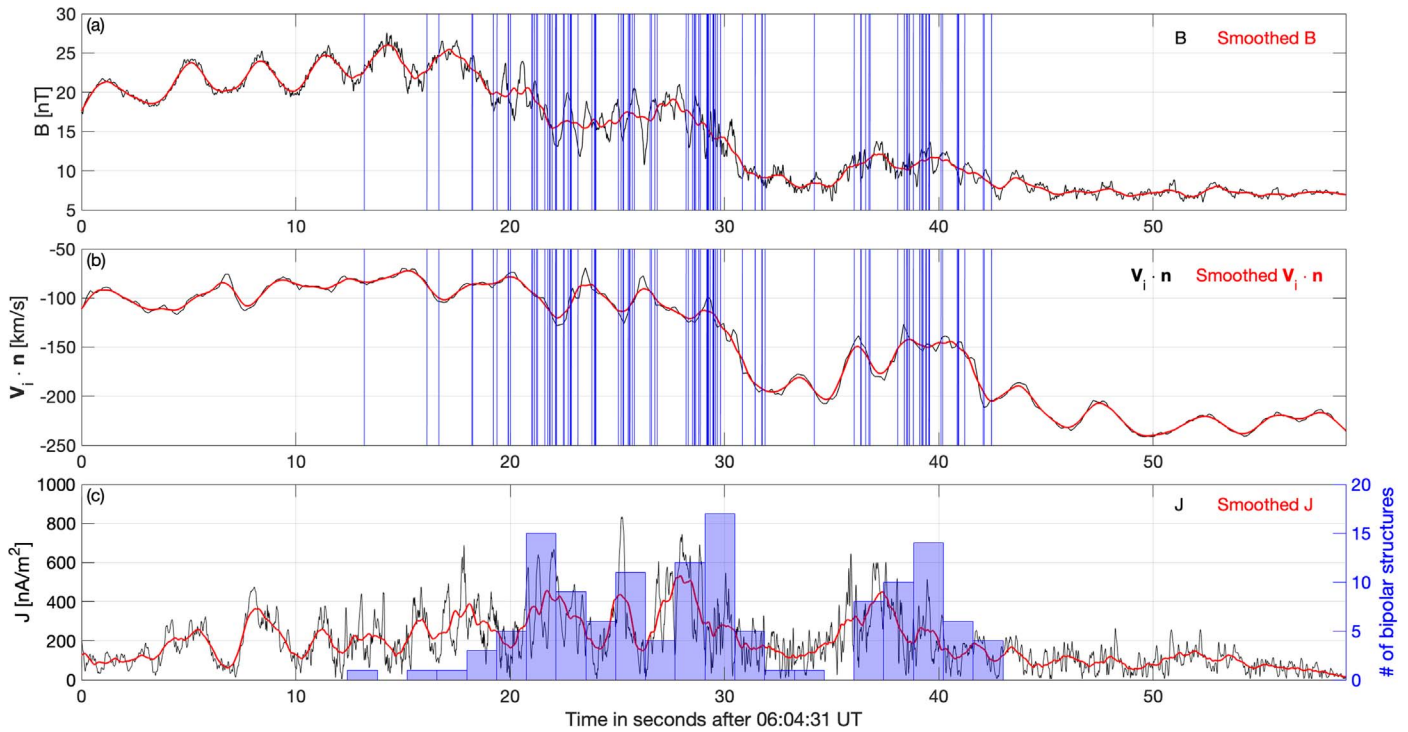
Figure 2. Analysis of occurrences of 134 bipolar electrostatic structures with amplitudes exceeding 50 mV m^{-1} that were selected using electric field measurements on board four *MMS* spacecraft: (a) the magnitude of the quasi-static magnetic field computed as an average value of the magnetic fields measured on board four *MMS* spacecraft (black) and its profile smoothed using a 1.5 s sliding window (red); the occurrence times (vertical lines) of the bipolar structures; (b) the ion bulk velocity (average value of ion bulk velocities measured on board four *MMS* spacecraft) along the shock normal **n** (black) and its profile smoothed using a 1.5 s sliding window (red); the occurrence times (vertical lines) of the bipolar structures; (c) the magnitude of the current density computed using simultaneous magnetic field measurements on board four *MMS* spacecraft (black) and its profile smoothed using a 1.5 s sliding window (red); the histogram presents the number of bipolar structures observed within bins of 1.5 s duration.

supercritical quasi-perpendicular shock with $T_e/T_i \approx 2.5$ and $\beta_i = 8\pi n T_i / B^2 \approx 0.8$ in the upstream region. In this regime the magnetic field in the shock transition region is rather turbulent in accordance with numerical simulations (e.g., Leroy et al. 1982; Scholer et al. 2003).

We have computed power spectral densities (PSDs) of electric and magnetic field fluctuations (8192 samples s^{-1}) using 0.1 s sliding window. The electric field PSD shown in panel (d) demonstrates the presence of broadband electric field fluctuations in the shock transition and downstream regions. The ratio between the electric and magnetic field PSDs shown in panel (e) indicates that the electric field fluctuations above a few hundred Hz tend to be electrostatic in accordance with previous measurements (Rodriguez & Gurnett 1975). Panel (f) shows that the electric field fluctuations in the shock transition region have amplitudes up to a few hundred mV m^{-1}. An expanded view of three electric field components measured over a highlighted 0.08 s interval demonstrates that some of the intense electric field fluctuations are due to bipolar electrostatic structures with a duration of a few milliseconds. A careful inspection through the electric field fluctuations with amplitudes exceeding 50 mV m^{-1} has resulted in a data set of 134 bipolar structures observed on board four *MMS* spacecraft. In what follows we focus on analysis of these large-amplitude bipolar structures.

Figure 2 presents analysis of the occurrence of the bipolar structures. Panel (a) shows that the bipolar structures occur predominantly in the shock transition region, and only a few bipolar structures are observed in the downstream region. In addition, the bipolar structures preferentially occur around the

magnetic field gradients. Panel (b), which presents the ion bulk velocity along the shock normal, demonstrates that the magnetic field gradients are associated with the slowing down of the ion bulk flow. Panel (c) presents the distribution of the bipolar structures that is obtained by counting the number of bipolar structures within bins of 1.5 s duration. In addition, panel (c) presents the magnitude of a local current density estimated using simultaneous magnetic field measurements on board four *MMS* spacecraft (see, e.g., Chanteur 1998 for methodology) along with its profile smoothed using a 1.5 s sliding window. The occurrence of the bipolar structures is well seen to be correlated with the local current density magnitude that is equivalent to the correlation with the magnetic field gradients in the shock transition region. This feature of the occurrence of bipolar structures in collisionless shocks is reported for the first time and will be discussed in the next section.

Figure 3 presents analysis of properties of a particular bipolar structure measured on board *MMS4*. The analysis is based on voltage signals induced on voltage-sensitive probes by the electric field of the bipolar structure (see Vasko et al. 2018 for methodology details). Panels (a) and (b) present voltage signals measured by two pairs of opposing probes on 60 m antennas in the spacecraft spin plane, while panel (c) presents voltage signals measured by the two opposing probes on 15 m axial antennas along the spin axis. Panel (d) presents components of the electric field **E** along the antenna directions computed using the voltage signals of the opposing probes. The time delays between the voltage signals of the opposing probes well noticeable in panels (a)–(c) allow the estimation of
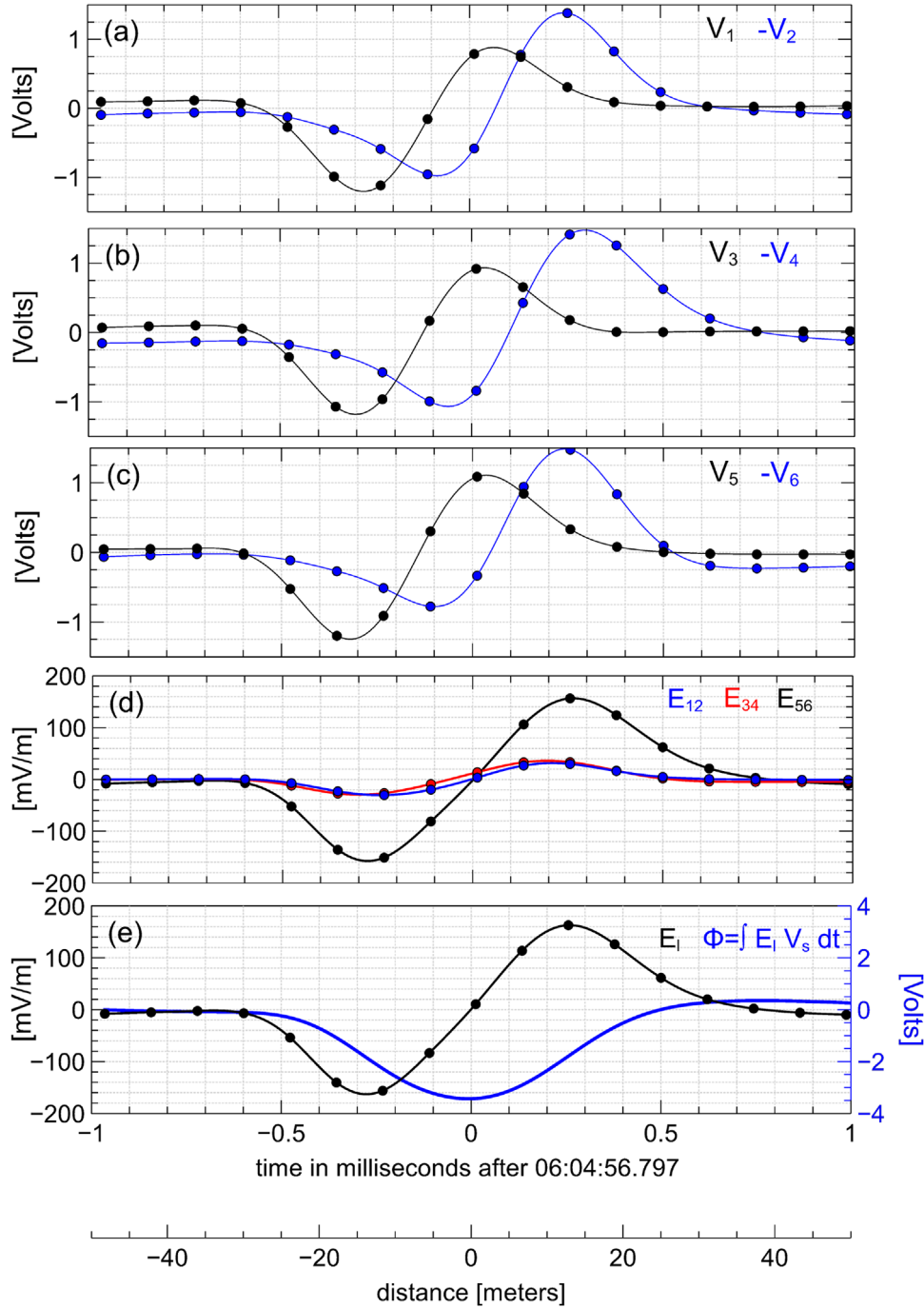
Figure 3. Analysis of properties of a particular bipolar structure measured on board *MMS4* that is based on voltage signals induced on six voltage-sensitive probes by the electric field of the bipolar structure (see Vasko et al. 2018 for methodology details): (a), (b) voltage signals V_1 vs. $-V_2$ and V_3 vs. $-V_4$ of the opposing probes mounted on 60 m antennas in the spacecraft spin plane; (c) voltage signals V_5 vs. $-V_6$ of the opposing probes mounted on 15 m axial antennas along the spin axis; the time delays between voltage signals of the opposing probes are used to compute the direction of propagation $\boldsymbol{k}$ and velocity V_s of the bipolar structure; (d) the electric field components E_{12}, E_{34}, and E_{56} along the antenna directions that were computed using the voltage signals of the opposing probes, $E_{ij} \propto (V_i - V_j)/(2l_{ij})$, where $l_{12} = l_{34} = 60$ m and $l_{56} = 15$ m are antenna lengths; (e) the electric field E_l of the bipolar structure (black) oriented a few degrees off the axial antenna (as one can infer from similar bipolar profiles in panel (d)); the electrostatic potential of the bipolar structure (blue) is computed as $\Phi = \int \boldsymbol{E} \cdot \boldsymbol{k} \, V_s \, dt$. In all panels dots represent measured quantities, while solid lines correspond to spline interpolated quantities. The electrostatic potential Φ is computed using the interpolated E_l profile. The lowest horizontal axis provides the spatial distance along the propagation direction $\boldsymbol{k}$ computed as $\int V_s dt$ and measured from $E_l = 0$.

velocity and direction of propagation of the bipolar structure. We have found that the bipolar structure propagates with velocity $V_s \approx 62 \, \text{km s}^{-1}$ along a unit vector $\boldsymbol{k}$ that is just a few degrees off the axial antenna. Interestingly, the bipolar structure propagates highly oblique to the shock normal, $\psi = \cos^{-1}(\boldsymbol{k} \cdot \boldsymbol{n}) \approx 90°$. Panel (d) shows that all three electric field components have similar bipolar profiles, while the electric field along the axial antenna is the dominant component. This indicates that the electric field of the bipolar structure is oriented a few degrees off the axial antenna direction. Panel (e) presents the electric field E_l in that direction, while the other two components are negligible
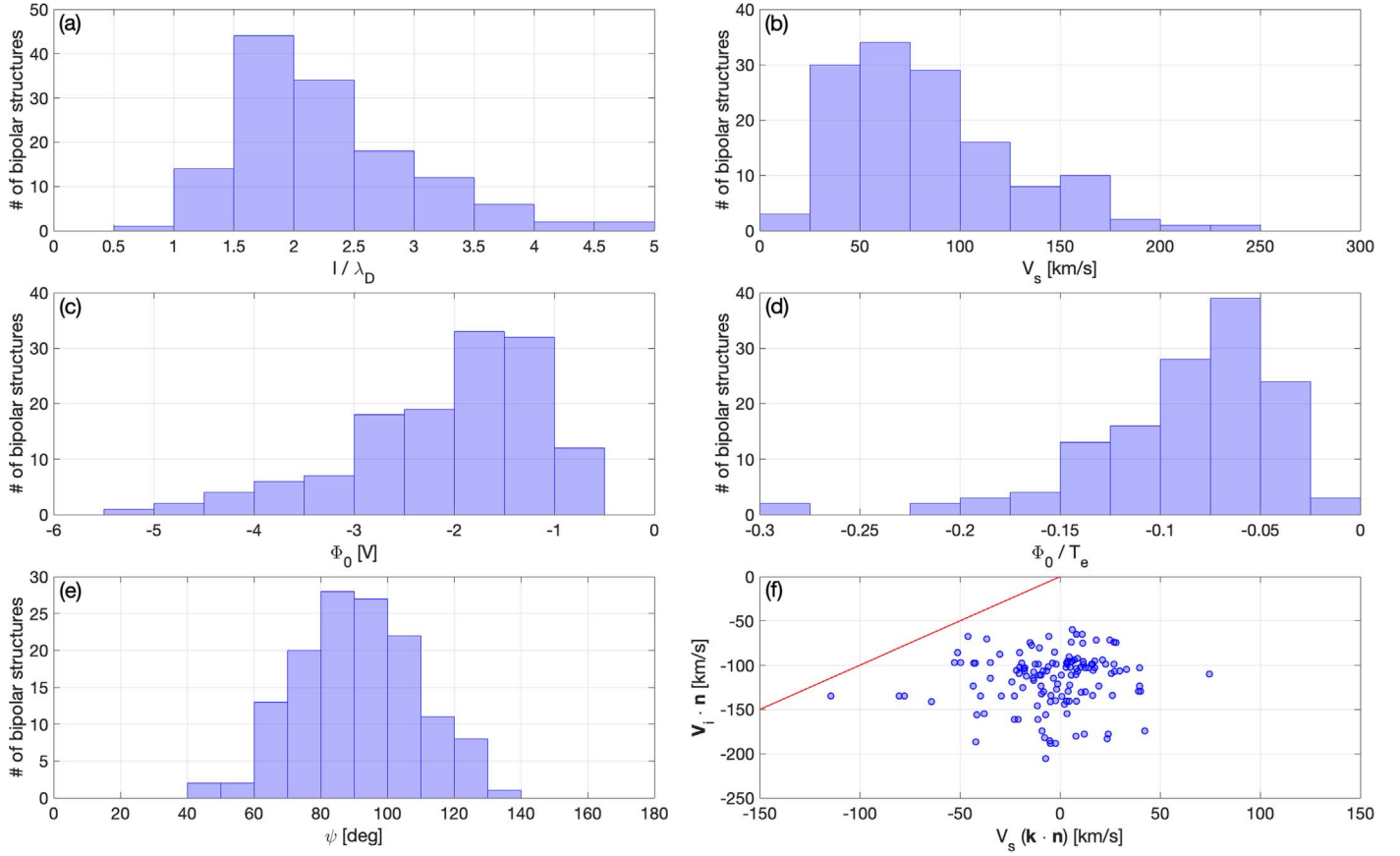
Figure 4. Summary of properties of 134 bipolar structures: (a) the spatial scale l in units of local Debye length λ_D; (b) the velocity V_s of the bipolar structures in the spacecraft reference frame; (c), (d) the amplitude Φ_0 of the electrostatic potential in physical units and in units of local electron temperature T_e; (e) the distribution of $\psi = \cos^{-1}(\mathbf{k} \cdot \mathbf{n})$, which is the angle between the propagation direction $\mathbf{k}$ of a bipolar structure and the shock normal $\mathbf{n}$; (f) the velocity of the bipolar structures along the normal, $V_s(\mathbf{k} \cdot \mathbf{n})$, vs. the normal component of the local ion bulk velocity, $V_i \cdot \mathbf{n}$; the red line corresponds to $V_s(\mathbf{k} \cdot \mathbf{n}) = V_i \cdot \mathbf{n}$. For all bipolar structures we observed $V_s (\mathbf{k} \cdot \mathbf{n}) > V_i \cdot \mathbf{n}$, which means that in the plasma rest frame the bipolar structures propagate toward the upstream region.

compared to E_l (not shown here). Because both $\mathbf{k}$ and $\mathbf{E}$ are approximately along the axial antenna, the angle between them is just a few degrees, indicating that the bipolar structure is approximately a 1D structure.

The estimated velocity of the bipolar structure allows the translation of temporal profiles into spatial profiles with a spatial coordinate along the propagation direction $\mathbf{k}$. The spatial coordinate measured from $E_l = 0$ is given below panel (e). We have computed the electrostatic potential of the bipolar structure as $\Phi = \int \mathbf{E} \cdot \mathbf{k} \, V_s \, dt$. Panel (e) shows that the bipolar structure has a negative electrostatic potential with a peak value $\Phi_0 \approx -3.5\,\mathrm{V}$ or $\Phi_0 \approx -0.1\,T_e$ in units of local electron temperature. We define the spatial scale l of the bipolar structure as $l = 0.5\,V_s\Delta t$, were Δt is the time interval between minimum and maximum values of E_l. Panel (e) shows that the spatial scale of the bipolar structure is $l \approx 16$ m or $l \approx 2\lambda_D$ in units of local Debye lengths. We have performed similar analysis of properties of all 134 bipolar structures and found that all of the bipolar structures have negative electrostatic potentials and hence cannot be interpreted in terms of electron phase space holes (e.g., Schamel 1986). We have also found that for more than 80% of the bipolar structures, the angle between $\mathbf{k}$ and $\mathbf{E}$ is within $30°$, so most of the bipolar structures are approximately 1D structures.

Figure 4 presents statistical distributions of the estimated parameters of the bipolar structures. Panel (a) shows that the bipolar structures have typical spatial scales of a few local

Debye lengths that is less than one-tenth of electron thermal gyroradius (not shown here). Panel (b) shows that bipolar structures commonly propagate with velocity around $100\,\mathrm{km\,s^{-1}}$ and higher velocities are rarer. In the plasma rest frame the velocities of the bipolar structures are of the order of the ion-acoustic velocity $c_s = (T_e/m_i)^{1/2} \sim 50\,\mathrm{km\,s^{-1}}$ that is much smaller than the electron thermal velocity (not shown here). Panels (c) and (d) show that the amplitudes of the electrostatic potential of the bipolar structures are typically a few Volts and within a few tenths of a local electron temperature. Panel (e) presents the distribution of $\psi = \cos^{-1}(\mathbf{k} \cdot \mathbf{n})$, which indicates that the bipolar structures propagate highly oblique to the shock normal: $60° \lesssim \psi \lesssim 120°$ for more than 90% of the structures. Panel (f) presents a comparison between $V_s(\mathbf{k} \cdot \mathbf{n})$, the velocity of bipolar structures along the shock normal, and $V_i \cdot \mathbf{n}$, the ion velocity component along the shock normal (see also Figure 2(b)). In the spacecraft frame the plasma flows toward the downstream region, $V_i \cdot \mathbf{n} < 0$, while the bipolar structures can propagate both toward the upstream, $\mathbf{k} \cdot \mathbf{n} > 0$, and downstream, $\mathbf{k} \cdot \mathbf{n} < 0$, regions. Interestingly, in the plasma rest frame, the bipolar structures propagate toward the upstream region, because as shown in panel (f) we observe $V_s(\mathbf{k} \cdot \mathbf{n}) > V_i \cdot \mathbf{n}$ for all bipolar structures. This feature of propagation direction of the bipolar structures is reported for the first time and will be discussed in the next section.

3. Interpretation

We have demonstrated that the large-amplitude bipolar structures observed in the shock transition region are Debye-scale structures with a negative electrostatic potential, propagating highly oblique to the shock normal. In the plasma rest frame, bipolar structures propagate toward the upstream region. The occurrence of bipolar structures is tightly correlated with magnetic field gradients in the shock transition region. These properties reveal the nature of the bipolar structures and instability driving them in the shock transition region.

The negative electrostatic potential of bipolar structures leads to the interpretation of these structures in terms of ion phase space holes, which are electrostatic structures formed in a nonlinear stage of various ion streaming instabilities (e.g., Schamel 1986; Kofoed-Hansen et al. 1989; Børve et al. 2001). Ion phase space holes are formed from ions trapped in potential wells of electrostatic fluctuations driven by instability. Regardless of the instability that produces bipolar structures in the shock transition region, there is a lowest increment value for that instability to be capable of producing the observed bipolar structures. Because the instability saturation occurs, when the bounce period of ions trapped within electrostatic fluctuations becomes comparable to an initial increment (e.g., Sagdeev & Galeev 1969), that increment γ should exceed the bounce frequency of ions trapped within bipolar structures, $\omega_b \approx l^{-1}(e|\Phi_0|/m_i)^{1/2}$, where m_i is the ion mass, l and Φ_0 are the spatial scale and amplitude of the electrostatic potential of a bipolar structure, respectively. We rewrite the criterion $\gamma \gtrsim \omega_b$ as follows:

$$\frac{\gamma}{\omega_{pi}} \gtrsim \frac{\lambda_{\mathrm{D}}}{l}\left(\frac{e|\Phi_0|}{T_e}\right)^{1/2}, \qquad (1)$$

where $\omega_{pi} = (4\pi n_0 e^2/m_i)^{1/2}$ is the ion plasma frequency. Adopting typical parameters of the observed bipolar structures, $l/\lambda_{\mathrm{D}} \sim 2$ and $e|\Phi_0|/T_e \sim 0.1$, we find that the initial increment should be of the order of a fraction of the ion plasma frequency, $\gamma \sim 0.1\,\omega_{pi}$.

The most plausible instability driving the observed bipolar structures is the ion two-stream instability between incoming and reflected ions (e.g., Akimoto & Winske 1985; Ohira & Takahara 2008). First, the observed strong correlation between the occurrence of the bipolar structures and magnetic field gradients indicates that reflected ions might be a source of free energy for the bipolar structures, because the reflection of a fraction of incoming ions is expected to occur due to magnetic field gradients (e.g., Leroy et al. 1982). The observed deceleration of the ion bulk flow associated with the magnetic field gradients is due to that reflection of incoming ions (Figure 2). Second, the ion two-stream instability is capable of explaining the observed properties of the bipolar structures and capable of providing the required linear increments.

Figure 5 presents a schematic of the ion two-stream instability in the shock transition region. Due to the reflection of a fraction of incoming ions by a magnetic field gradient, the ion distribution function is locally a combination of incoming ions with density n_0 and reflected ions with density n_{ref}. In the normal incidence frame the bulk velocity of incoming ions is $-V_n\,\boldsymbol{n}$, where $V_n = |V_i \cdot \boldsymbol{n} - V_{\mathrm{sh}}|$ and V_{sh} is the shock velocity and $\boldsymbol{n}$ the shock normal. In the reference frame of incoming ions, reflected ions propagate along the shock normal (toward upstream) with velocity $\boldsymbol{V}_{\mathrm{ref}} = V_{\mathrm{ref}}\,\boldsymbol{n} = 2V_n\,\boldsymbol{n}$. The simplest
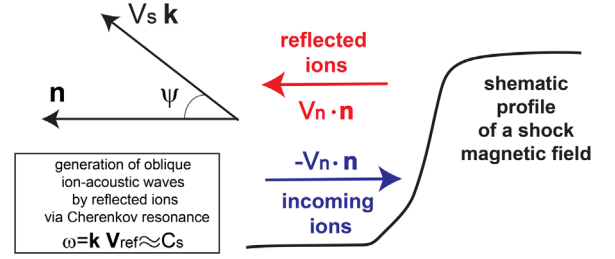

Figure 5. Schematic of the ion two-stream instability between incoming and reflected ions in the shock transition region. In the normal incidence frame the bulk velocity of incoming ions is $-V_n\,\boldsymbol{n}$, where $V_n = |V_i \cdot \boldsymbol{n} - V_{\mathrm{sh}}|$, V_{sh} is the shock velocity and $\boldsymbol{n}$ is the shock normal. In the frame of incoming ions the reflected ions propagate upstream with velocity $\boldsymbol{V}_{\mathrm{ref}} = 2V_n\,\boldsymbol{n}$. The reflected ions are capable of driving ion-acoustic waves satisfying the Cerenkov resonance, $\omega = \boldsymbol{k} \cdot \boldsymbol{V}_{\mathrm{ref}}$, where frequency ω and wavevector $\boldsymbol{k}$ are related to each other by the ion-acoustic wave dispersion relation. In the rest frame of incoming ions the ion-acoustic waves propagate toward the upstream region, have wavelengths of a few Debye lengths and propagate oblique to the shock normal at an angle ψ satisfying $\cos\psi \approx c_s/V_{\mathrm{ref}}$, where c_s is the ion-acoustic velocity. In a nonlinear stage of the instability the ion-acoustic waves transform into ion phase space holes (e.g., Kofoed-Hansen et al. 1989; Børve et al. 2001 for simulations). The ion phase space holes inherit the properties of the ion-acoustic waves: propagate in the direction of reflected ions, which is toward the upstream region (in the rest frame of incoming ions), have wavelengths of the order of a few Debye lengths, and propagate highly oblique to the shock normal.

analysis of the instability between incoming and reflected ions was presented by Akimoto & Winske (1985) and Ohira & Takahara (2008) by assuming cold ion populations and neglecting effects of the magnetic field (that is reasonable for waves with wavelengths much smaller than electron and ion thermal gyroradii, which is the case for Debye-scale waves). That analysis showed that reflected ions drive ion-acoustic waves satisfying the Cerenkov resonance

$$\omega \approx \boldsymbol{k}V_{\mathrm{ref}} = V_{\mathrm{ref}}(\boldsymbol{k} \cdot \boldsymbol{n}) = kV_{\mathrm{ref}}\cos\psi, \qquad (2)$$

where ψ is the angle between $\boldsymbol{k}$ and $\boldsymbol{n}$, and frequency ω and wavevector $\boldsymbol{k}$ are approximately related by the dispersion relation of ion-acoustic waves

$$\omega \approx \omega_{pi}k\lambda_{\mathrm{D}}/(1 + k^2\lambda_{\mathrm{D}}^2)^{1/2}. \qquad (3)$$

The fastest-growing ion-acoustic waves have wavelengths of a few Debye lengths, $k\lambda_{\mathrm{D}} \sim 1$, and the increment dependent on the fraction of reflected ions

$$\frac{\gamma_{\max}}{\omega_{pi}} \approx \left(\frac{3\sqrt{3}}{16}\frac{n_{\mathrm{ref}}}{n_0}\right)^{1/3}. \qquad (4)$$

The resonance condition $\omega \approx kV_{\mathrm{ref}}\cos\psi$ shows that the fastest-growing ion-acoustic waves propagate oblique to the shock normal

$$\cos\psi \approx \omega/kV_{\mathrm{ref}} \approx c_s/V_{\mathrm{ref}}, \qquad (5)$$

where $c_s = \omega_{pi}\lambda_{\mathrm{D}} = (T_e/m_i)^{1/2}$ is the ion-acoustic velocity. Thus, ion-acoustic waves produced by the instability between incoming and reflected ions: (1) propagate in the direction of reflected ions, that is, toward the upstream region (in the rest frame of incoming ions); (2) have wavelengths of the order of a few Debye lengths; (3) propagate oblique to the shock normal.

The properties (1)–(3) above are consistent with the observed parameters of the bipolar structures. We have found that the bipolar structures propagate toward the upstream region in the plasma rest frame. In that frame, the incoming

ions propagate toward the downstream region, while reflected ions propagate upstream. Therefore, in the rest frame of incoming ions, the bipolar structures also propagate toward the upstream region that is in accordance with (1). The bipolar structures have spatial scales of a few Debye lengths and propagate oblique to the shock normal that is in accordance with (2) and (3). The observed highly oblique propagation results from the Cerenkov resonance condition, $\cos\psi \approx c_s/V_{\rm ref}$, where $c_s = (T_e/m_i)^{1/2}$ is of the order of 50 km s^{-1}, $V_{\rm ref} = 2\,|V_i \cdot \boldsymbol{n} - V_{\rm sh}|$ is in the range from 400 to 120 km s^{-1}, because $V_{\rm sh} \approx -38$ km s^{-1}, and $V_i \cdot \boldsymbol{n}$ is in the range from -250 to -100 km s^{-1} (Figure 2). Finally, according to Equation (4) for typical densities of reflected ions, $n_{\rm ref} \sim 0.1\,n_0$ (Leroy et al. 1982; Scholer et al. 2003), the ion two-stream instability can provide initial increments of a fraction of the ion plasma frequency as required by Equation (1).

We have assumed both incoming and reflected ions to be cold. Finite ion temperatures would affect the instability characteristics quantitatively, but not the most critical features of the ion two-stream instability (Gary & Omidi 1987): propagation in the same direction as reflected ions (in the rest frame of incoming ions), wavelengths of a few Debye lengths, and highly oblique propagation to the shock normal. Therefore, we consider our interpretation to be robust, though a detailed analysis of the ion velocity distribution function should be performed in the future to resolve reflected ions (not necessarily specularly reflected as assumed in the simplest scenario) to test the Cerenkov resonance condition (2) and (5).

4. Discussion

The bipolar structures in the Earth's bow shock were originally interpreted in terms of electron phase space holes, which are electrostatic structures produced in a nonlinear stage of various electron streaming instabilities (Bale et al. 1998, 2002). The potential instabilities were electron two-stream (e.g., Gedalin 1999) and beam (e.g., Thomsen et al. 1983) instabilities. However, the recent analysis of about 20 bipolar structures in a particular Earth's bow shock crossing showed that the bipolar structures cannot be electron phase space holes, because they have a negative electrostatic potential (Vasko et al. 2018). In this Letter we have considered an Earth's bow shock crossing with more than 100 bipolar structures in the shock transition region and confirmed that the bipolar structures cannot be electron phase space holes. Based on the detailed analysis, we have interpreted the bipolar structures in terms of ion phase space holes produced by the instability between incoming and reflected ions. That is the first experimental evidence that the ion two-stream instability produces the electrostatic turbulence in collisionless shocks.

The ion two-stream instability between incoming and reflected ions was suggested by Formisano & Torbert (1982) and Akimoto & Winske (1985), while Ohira & Takahara (2008) have recently revived interest to that instability. The 2D particle-in-cell (PIC) simulations of the ion two-stream instability evolution in a uniform plasma have demonstrated ion heating and practically no electron heating or acceleration (Ohira & Takahara 2008). However, as discussed below, we cannot rule out that in a realistic nonuniform shock configuration, the electrostatic turbulence driven by the ion two-stream instability is capable of accelerating a fraction of thermal electrons to superthermal energies.

The 2D PIC simulations by Ohira & Takahara (2007) showed that in a uniform plasma the electrostatic turbulence driven by the Buneman instability (typical of high Mach number shocks) is incapable of accelerating electrons via the surfing mechanism demonstrated by 1D simulations (Hoshino & Shimada 2002). On the contrary, the 2D PIC simulations of Amano & Hoshino (2009), which included a realistic nonuniform shock configuration, demonstrated that the Buneman instability can provide electron acceleration via the stochastic surfing acceleration (SSA) mechanism. In the SSA mechanism electrons are accelerated to superthermal energies due to multiple interactions with the electrostatic turbulence in the upstream region, which are possible due to electron mirroring by a nonuniform magnetic field of the shock.

The recent 2D PIC simulations by Umeda et al. (2009) have demonstrated that the SSA mechanism can also operate at low Mach numbers typical of the Earth's bow shock. In those simulations the electrostatic turbulence is produced by reflected ions. Although Umeda et al. (2009) did not dwell on the nature of the instability, the most plausible case is the ion two-stream instability. The identification of the ion two-stream instability presented in this Letter and simulations by Umeda et al. (2009) indicate that the electrostatic turbulence produced by that instability can provide electron acceleration in collisionless shocks via the SSA mechanism.

5. Conclusion

The analysis of more than 100 bipolar structures in a supercritical quasi-perpendicular Earth's bow shock showed that the bipolar structures are ion phase space holes produced by the two-stream instability between incoming and reflected ions. The arguments supporting this interpretation are:

1. The bipolar structures have negative amplitudes of the electrostatic potential and spatial scales of a few Debye lengths.
2. The occurrence of the bipolar structures is correlated with the magnetic field gradients capable of reflecting a fraction of incoming ions.
3. In the shock rest frame the bipolar structures propagate highly oblique to the shock normal, the angle between the propagation direction and the shock normal is within $(60°, 120°)$ for more than 90% of the bipolar structures.
4. In the plasma rest frame the bipolar structures propagate toward the upstream region, that is, in the direction of propagation of reflected ions.
5. The ion two-stream instability is capable of providing the required increments of a fraction of the ion plasma frequency.

That is the first demonstration that the ion two-stream instability produces the electrostatic turbulence in supercritical collisionless shocks.

ORCID iDs

R. Wang https://orcid.org/0000-0002-6463-7364
I. Y. Vasko https://orcid.org/0000-0002-4974-4786
F. S. Mozer https://orcid.org/0000-0002-2011-8140
S. D. Bale https://orcid.org/0000-0002-1989-3596
C. T. Russell https://orcid.org/0000-0003-1639-8298

References

Akimoto, K., & Winske, D. 1985, JGR, 90, 12095
Amano, T., & Hoshino, M. 2009, ApJ, 690, 244
Bale, S. D., Hull, A., Larson, D. E., et al. 2002, ApJL, 575, L25
Bale, S. D., Kellogg, P. J., Larsen, D. E., et al. 1998, GeoRL, 25, 2929
Balikhin, M., Walker, S., Treumann, R., et al. 2005, GeoRL, 32, L24106
Bamba, A., Yamazaki, R., Ueno, M., & Koyama, K. 2003, ApJ, 589, 827
Børve, S., Pécseli, H. L., & Trulsen, J. 2001, JPlPh, 65, 107
Burch, J. L., Moore, T. E., Torbert, R. B., & Giles, B. L. 2016, SSRv, 199, 5
Cargill, P. J., & Papadopoulos, K. 1988, ApJL, 329, L29
Chanteur, G. 1998, ISSIR, 1, 349
Ergun, R. E., Tucker, S., Westfall, J., et al. 2016, SSRv, 199, 167
Formisano, V., & Torbert, R. 1982, GeoRL, 9, 207
Gary, S. P., & Omidi, N. 1987, JPlPh, 37, 45
Gedalin, M. 1999, GeoRL, 26, 1239
Goodrich, K. A., Ergun, R., Schwartz, S. J., et al. 2018, JGRA, 123, 9430
Gosling, J. T., Thomsen, M. F., Bame, S. J., & Russell, C. T. 1989, JGR, 94, 10011
Hoshino, M., & Shimada, N. 2002, ApJ, 572, 880
Hull, A. J., Larson, D. E., Wilber, M., et al. 2006, GeoRL, 33, L15104
Hutchinson, I. H. 2017, PhPl, 24, 055601
Kennel, C. F., Edmiston, J. P., & Hada, T. 1985, GMS, 34, 1
Kofoed-Hansen, O., Pecseli, H. L., & Trulsen, J. 1989, PhyS, 40, 280
Le Contel, O., Leroy, P., Roux, A., et al. 2016, SSRv, 199, 257
Leroy, M. M., Winske, D., Goodrich, C. C., Wu, C. S., & Papadopoulos, K. 1982, JGRA, 87, 5081
Lindqvist, P.-A., Olsson, G., Torbert, R. B., et al. 2016, SSRv, 199, 137
Mozer, F. S., & Sundkvist, D. 2013, JGRA, 118, 5415
Ohira, Y., & Takahara, F. 2007, ApJL, 661, L171
Ohira, Y., & Takahara, F. 2008, ApJ, 688, 320
Oka, M., Terasawa, T., Seki, Y., et al. 2006, GeoRL, 33, L24104
Oka, M., Wilson, L. B., Phan, T. D., et al. 2017, ApJL, 842, L11
Papadopoulos, K. 1985, GMS, 34, 59
Pollock, C., Moore, T., Jacques, A., et al. 2016, SSRv, 199, 331
Rodriguez, P., & Gurnett, D. A. 1975, JGR, 80, 19
Russell, C. T., Anderson, B. J., Baumjohann, W., et al. 2016, SSRv, 199, 189
Sagdeev, R. Z., & Galeev, A. A. 1969, Nonlinear Plasma Theory (New York: Benjamin)
Schamel, H. 1986, PhR, 140, 161
Schmitz, H., Chapman, S. C., & Dendy, R. O. 2002, ApJ, 579, 327
Scholer, M., Shinohara, I., & Matsukiyo, S. 2003, JGRA, 108, 1014
Shimada, N., & Hoshino, M. 2004, PhPl, 11, 1840
Thomsen, M. F., Barr, H. C., Gary, S. P., Feldman, W. C., & Cole, T. E. 1983, JGR, 88, 3035
Umeda, T., Yamao, M., & Yamazaki, R. 2009, ApJ, 695, 574
van Weeren, R. J., Röttgering, H. J. A., Brüggen, M., & Hoeft, M. 2010, Sci, 330, 347
Vasko, I. Y., Mozer, F. S., Krasnoselskikh, V. V., et al. 2018, GeoRL, 45, 5809
Vinas, A. F., & Scudder, J. D. 1986, JGR, 91, 39
Wilson, L. B., Sibeck, D. G., Breneman, A. W., et al. 2014, JGRA, 119, 6475